Nanoparticle-coated Vivaldi Antenna Array for Gain Enhancement

Pouya Faeghi[1,2*], Changiz Ghobadi[1,2], Javad Nourinia[1,2], Bal Virdee[3]
[1] Department of Electrical Engineering, Urmia University, Urmia 5756151818, Iran.
[2] Northwest antenna and microwave research laboratory (NAMRL), Urmia University, Urmia, Iran.
[3] Center for Communications Technology, School of Computing & Digital Media, London Metropolitan University, London N7 8DB, UK.

* Correspondence author: pouya.faeghi@gmail.com

Abstract
A novel technique is described to significantly enhance the gain of a Vivaldi antenna (CVA) array by a factor of four (6 dB) without compromising its size and radiation characteristics. This is achieved by loading the antenna with Complementary Split Ring Resonators (CSRR) and periodic array of open loop meander-line unit cells. The unit cells are designed to exhibit properties of anisotropic zero-index metamaterial (AZIM) over a frequency range of the antenna. The inclusion of CSRR and AZIM in the antenna design is shown to effectively expand its aperture size with the advantage of not impacting on the overall size of the antenna. Moreover, the antenna is excited with a novel feedline consisting of hair-comb radial-stubs (HCRS) that matches the impedance the 50-Ω feedline with the radiating elements of the antenna to thereby maximize power transfer. The proposed antenna array was fabricated to validate its performance. The peak measured gain of the array is 7.49 dBi at 177 degrees in the E-plane and its sidelobes are 10 dB below the peak gain. The 3-dB beamwidth of the array is 32.8 degrees. Furthermore, it is shown for the first time that by depositing a thin film of Graphene/copper nanoparticles onto the CSRR, the array's gain is increased to 10 dBi at 180 degrees with sidelobe reduction of better than 15 dB.

Keywords Conventional Vivaldi antenna, miniaturization, gain enhancement, metamaterial, hair-comb radial-stub feed

1 Introduction

Different arrangements of metamaterial unit cells have been integrated to develop printed antennas such as Tapered Slot Microstrip Antenna (TSMA) with enhanced performance [1,2]. Planar antenna such as microstrip Vivaldi antenna offers the benefits of accommodating metamaterial structures on the top or bottom layer. The salient feature of Vivaldi antenna is high front-to-back ratio (FTB) in the radiation pattern [3,4]. Previously the gain, impedance, FTB, and sidelobe level ratio (SLL) of planar antenna have been improved by either employing certain substrates [4] or using specific array structures or embedding photonic bandgap (PBG) artifacts or metamaterial inclusions [5-8]. The current approaches can be structurally complex to design and implement thereby having an impact on fabrication cost.

In the literature you can find several Vivaldi antennas with various configurations for numerous applications including Ground Penetrating Radar (GPR) [9], tumor detection [10], and Ultra-Wide Band (UWB) communication [11,12]. The use of Split-Ring Resonators (SRR) in the design of the Vivaldi antenna is not new. The purpose of SSRs is essentially to generate multiple resonances over the operating range of the antenna. Although SRR have been shown to improve the antenna's radiation efficiency and impedance bandwidth, but this is at the expense of gain performance [12,13]. In [14-17] complementary SRR (CSRR) and Anisotropic Zero Index Metamaterial (AZIM) unit cells have been utilized in the aperture of the Vivaldi antenna to alter the surface current distribution over the antenna thereby boosting the antenna's gain performance. However, the SRR loading has a detrimental on the overall gain of the antenna especially at the resonating frequency corresponding to the SRR structure. Hence, reduction of the overall gain of Vivaldi antenna is one of the fundamental issues when using an SRR structure.

Recent advances in nanotechnology have produced breakthroughs in high-quality low-cost Graphene production [18]. Nanomaterials such as Graphene nanocomposites provide superior thermal, electrical, and mechanical characterizations with a high surface area, making it an amplifying material for antenna array [19-21]. Furthermore, Graphene oxide nanoparticles can be deposited on metal carbides or metal surfaces through chemical vapor deposition and wet chemical synthesis [22,23]. Graphene nanoplatelets (GnP) comprising 10-30 layers of Graphene oxide have been exploited in the combination of screen-printing technology and rolling compression to develop GnPs-based radio frequency flexible antenna [24].

In this paper, a combination of CSRR and AZIM metamaterial unit cells are used to enhance the gain performance of CVA. In the proposed technique a novel feedline coupling structure is employed to optimize the impedance matching with the antenna to maximize power transfer. Furthermore, the deposition of a thin film of Graphene film over the metallization sections of the antenna is shown to significantly improve the gain and radiation characteristics. This represents a new paradigm for the design and realization of Graphene-based antennas.

2 Antenna Design

Fig. 1(a), shows a conventional Vivaldi antenna (CVA) and the excitation mechanism on the opposite side of the dielectric substrate, which is a radial stub. The physical parameters of the standard reference antenna were obtained using the design equations in [14]. Fig. 1(b) shows the proposed excitation mechanism, which consists of hair-comb radial-stub (HCRS). Fig. 1(d) shows the array implemented with HCRS. The current density distribution over the conventional radial-stub and the proposed hair-comb radial-stub are shown in Fig. 1(d). The current is uniformly distributed over the proposed HCRS mechanism. The current density was obtained using a three-dimensional electromagnetic solver called CST Microwave Studio.

The proposed excitation structure used here effectively matches the 50-Ω feedline impedance with the antenna for optimum electromagnetic coupling which contributes to maximizing the power transfer to and from the wireless transceiver. This is important to reduce energy wastage. The antenna array in Fig. 1c is excited using a 1-to-4 Wilkinson Power Divider (WPD) constructed on the bottom substrate layer. The standard WPD is used and consists of a T-shaped splitter with 100-Ω resistor connecting the two output ports for matching purposes and for isolating the ports at the center frequency. Fig. 2 shows the return-loss and insertion-loss response of the Wilkinson Power Divider. The antennas are constructed on standard Rogers substrate (RO4003C) with a loss-tangent of 0.0027 and a thickness of 0.8 mm. The initial dimensions of the antenna array design are $57.50\times45\times0.8$ mm^3. After optimization the final dimensions of the array antenna are $95.25\times190\times0.8$ mm^3.

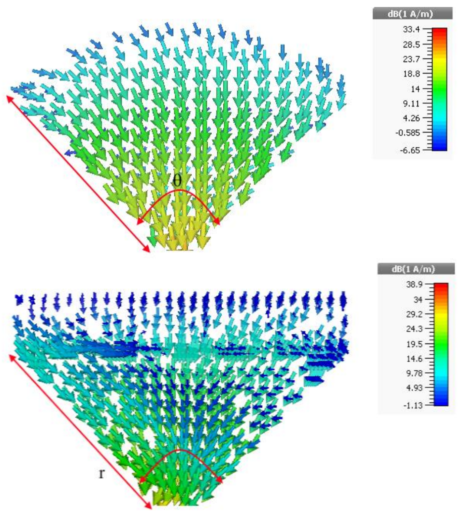

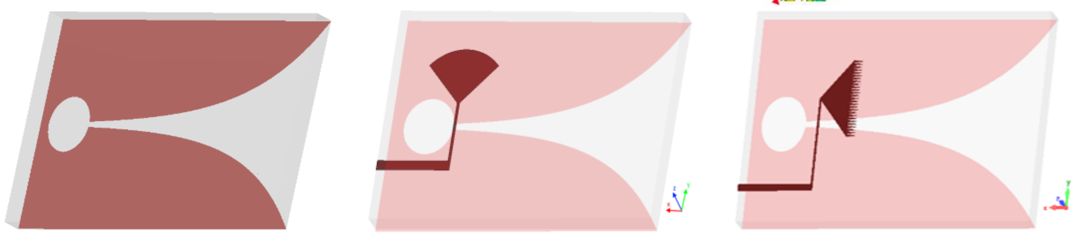

(a)

(b)

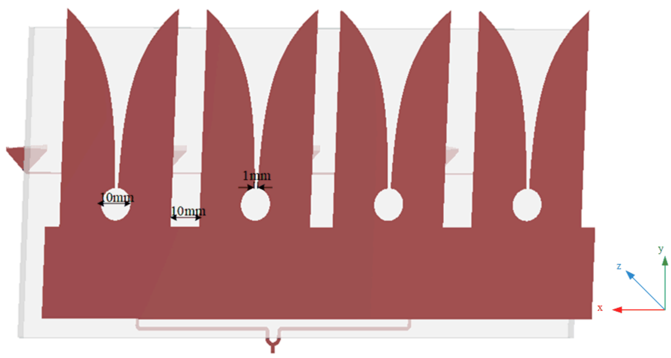

(c)

(d)

Fig. 1. (a) Conventional Vivaldi antenna (Ant. 1), (b) Vivaldi antenna with hair-comb radial-stub (Ant. 2), the exponential slot curve is determined by $Y_x = ae^{bx} + c$ where $0 \leq x$, (c) Four-element array (Ant. 3), and (d) current density distribution over the hair-comb frontal radial-stub.

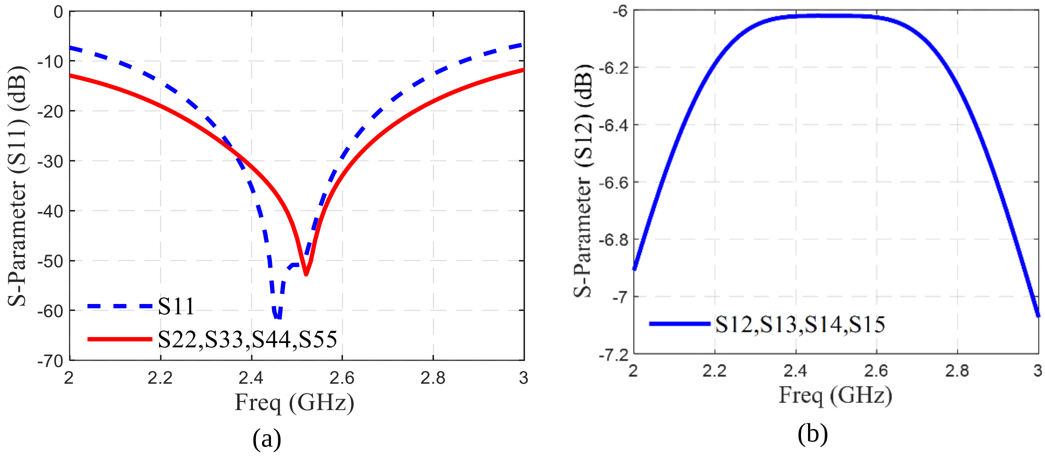

Fig. 2. Simulated response of a 5-port WPD, (a) Return-loss, and (b) Insertion-loss.

The value of capacitance (*C*) and inductance (*L*) of the hair-comb radial-stub can be calculated using [25]

$$C_{HCRS} \cong \frac{\theta r^2 \varepsilon_{eff}}{240\pi hc} \qquad (1)$$

$$L_{HCRS} \cong \frac{120\pi h}{\theta c}(\ln r - 0.5) \qquad (2)$$

where h is dielectric substrate thickness, radial angle $\theta = 90^\circ$, ε_{eff} is effective dielectric constant, r is radius of radial stub and c is speed of light.

2.1 Miniaturization

The operating frequency for a microstrip antenna loaded with metamaterial based on given dielectric material is inversely proportional to its refractive index (n_{ref}). Consequently, the length of the antenna at its fundamental resonant frequency (f_o) can be determined from [26]:

$$L_{MM} \approx \frac{c}{2f_0 n_{ref}} \qquad (3)$$

The miniaturization feature of the antenna is defined by the Compact Factor (*CF*), which is the profile ratio of the circuit without metamaterial in comparison to circuit with metamaterial, and is given by:

$$CF = \frac{\varepsilon_{ref}}{|\varepsilon_{eff}\mu_{eff}|} \qquad (4)$$

Where μ_{eff} and ε_{eff} are the effective permittivity and permeability of the metamaterial, respectively. Then to miniaturize the antenna, *CF* needs to be <1. Therefore, the parameters μ_{eff} and ε_{eff} are required to be obtained in which $\varepsilon_{eff} < \varepsilon_{ref}$. The miniaturization needs good impedance matching without trading off the performance of the antenna. In the next section, a metamaterial unit cell structure is determined to load the Vivaldi antenna for the purpose of improving its gain performance [27].

2.2 *Metamaterial Unit Cell*

Here the CSRR unit cell is placed on the HCRS, as shown in Fig. 3, for optimum electromagnetic coupling. The CSRR unit cell is positioned near the feed point to excite it with the normal electric field component. The position of the proposed CSRR unit cell is optimized to optimize the signal rejection. The transmission properties of this structure were investigated using full-wave numerical analysis using CST Microwave Studio and by applying appropriate boundary conditions and Floquet port excitation. Simulation results, in Fig. 4, confirm the group and phase velocities of the main wave to be travel in opposite directions to realize negative refractive index, which is characteristic of metamaterials, i.e., $v_p = -\omega^2\sqrt{LC}$, and $v_g = +\omega^2\sqrt{LC}$ [28]. Therefore $v_p v_g = -\omega^4 LC \neq c^2$. Resulting in a negative refractive index

$n = \frac{c}{v_p}$, $v_p < 0 \to n < 0$. Hence, $\varepsilon < 0 \to \varepsilon = \varepsilon_0\left(1 - \frac{\omega_p^2}{\omega^2 - j\omega\gamma}\right)$, $n = -j\sqrt{\mu_r|\varepsilon_r|}$.

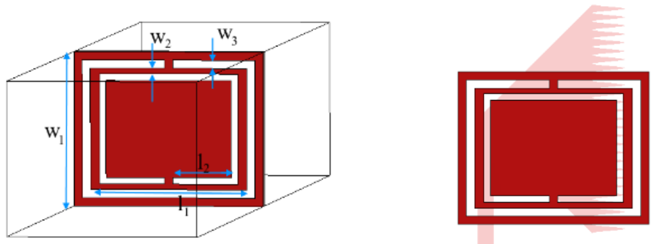

(a)

(b)

Fig. 3. (a) CSRR unit cell; and (b) CSRR unit cell located close to HCRS. The dimensions are: l_1=9.56 mm, l_2=3.61 mm, w_1=8.35 mm, w_2=0.33 mm, & w_3=0.5 mm.

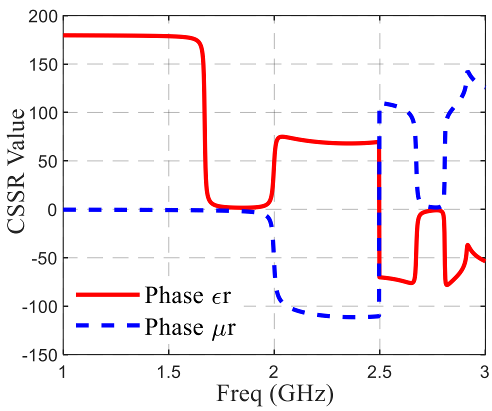

Fig. 4. Phase (degrees) of backward-wave propagation in the CSRR.

The effect of CSRR loading on the Vivaldi antenna is indicated by the current distribution over it in Fig. 5 at various impinging field phase angles. It is clear from this figure that at phase angles of 60, 180, 240 and 360 degrees the current distribution over the CSRR is most intense. Fig. 6 shows the CSSR real and imaginary components permittivity and permeability as a function of frequency. According to the diagram in Fig.6, permeability has negative values in the frequency range of 2 to 2.5 GHz (real and imaginary). Over the same frequency range, the imaginary component of the permittivity is positive, and the value of the real component is close to zero.

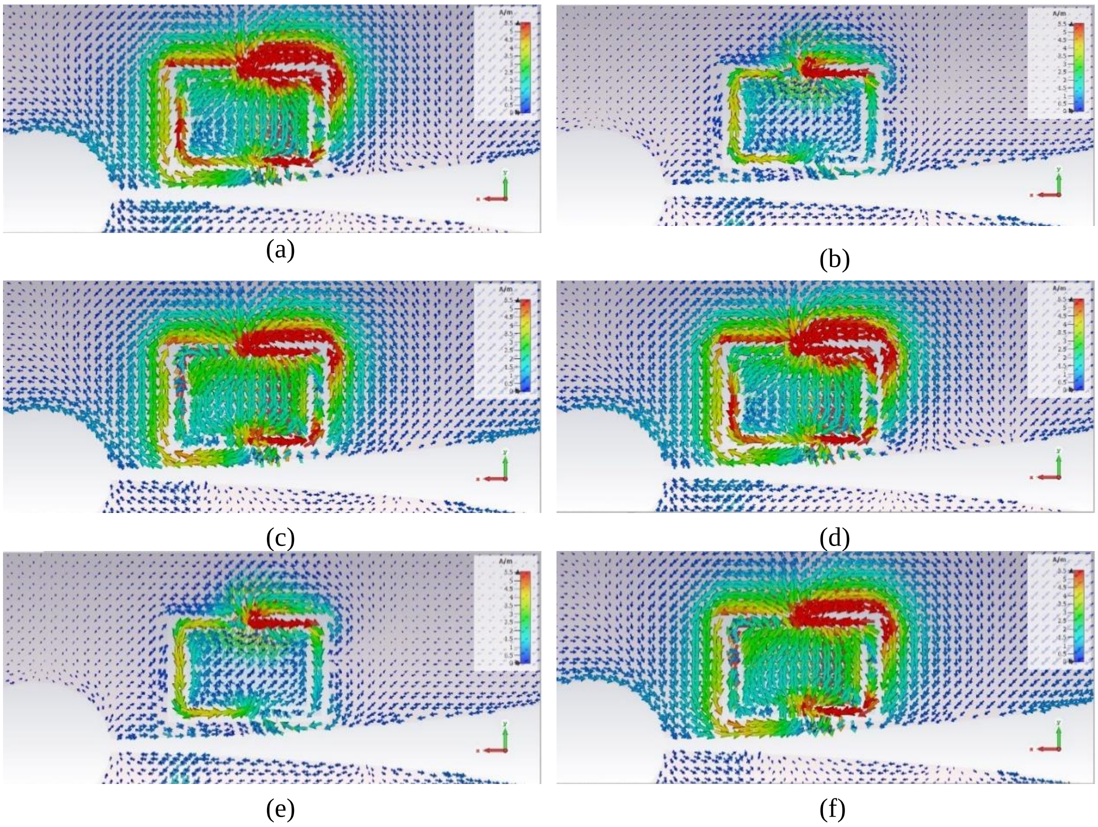

Fig. 5. Current density distribution showing the effect of CSRR loading at its resonant frequency of 2.45 GHz and at phase angles of: (a) 60 degrees, (b) 120 degrees, (c) 180 degrees, (d) 240 degrees, (e) 300 degrees, and (f) 360 degrees.

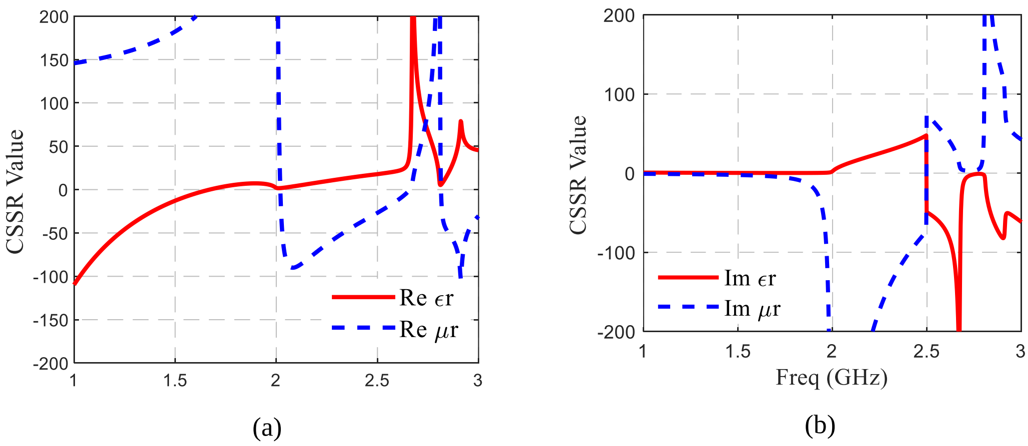

Fig. 6. Permittivity and permeability of the proposed structure comprising CSRR unit cell and HCRS; (a) Real ε_r, μ_r; and (b) Imaginary ε_r, μ_r.

The directivity of the CSRR loaded Vivaldi antenna is improved by incorporating AZIM unit cells whose open-loop meander-line structure is shown in Fig. 7. The dimensions of the AZIM unit cell were optimized with the help of CST Microwave Studio, which is a 3D electromagnetic solver. The effective relative permittivity of the AZIM unit cell along the direction of beam radiation is shown in Fig. 8. The permittivity was calculated using a MATLAB program based on the standard retrieval procedure [28]. Fig. 8 shows this simple structure exhibits characteristics of AZIM

($\mu_{\mathrm{Re}} < 0, \mu_{\mathrm{Im}} < 0$) over a certain frequency range which is dictated by its dimensions. The effective relative permittivity is near zero within the frequency range of 1.7 to 2.2 GHz. The phase of backward-wave propagation in the AZIM is shown in Fig. 9.

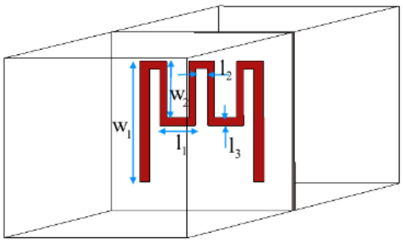

Fig. 7. Open-loop meander-line AZIM unit cell.

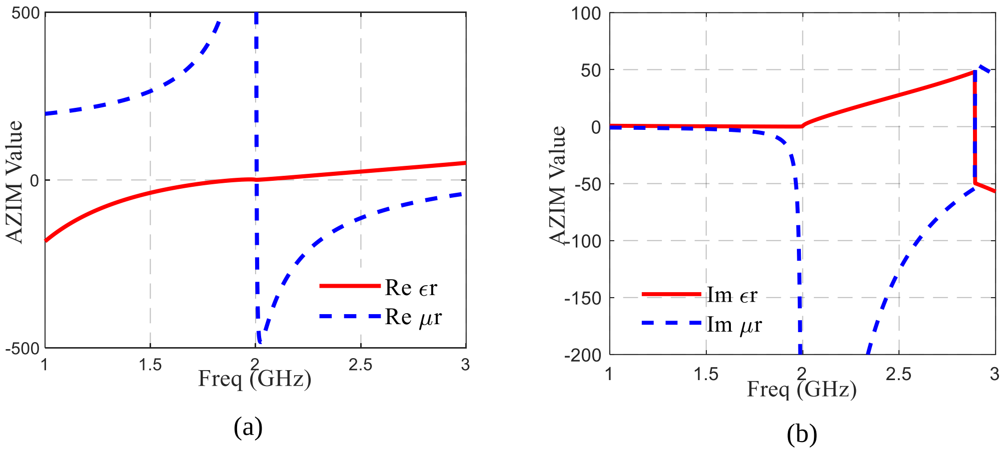

Fig. 8. Meander line AZIM unit cell, (a) Real ε_r, μ_r, and (b) Imaginary ε_r, μ_r.

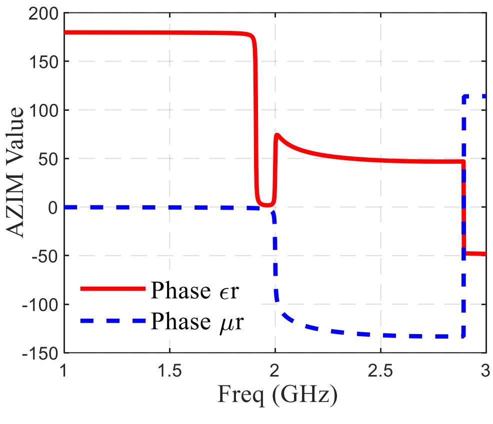

Fig. 9. Phase (degrees) of backward-wave propagation in the AZIM structure.

3 Graphene Layer

Graphene is made from carbon atoms in a hexagonal lattice ordered in a single atomic sheet. The Hamiltonian of Graphene due to the firm bond model can be written as:

$$H = -t \sum_i a_{r_i}^{+} b_{r_i+e_1} - t \sum_i a_{r_i}^{+} b_{r_i+e_2} - t \sum_i a_{r_i}^{+} b_{r_i+e_3} + \text{Hermitian conjugate} \qquad (5)$$

where $e_1 = (0, a)$, $e_2 = \left(\frac{-\sqrt{3}a}{2}, \frac{-a}{2}\right)$, $e_3 = \left(\frac{\sqrt{3}a}{2}, \frac{-a}{2}\right)$, a is the length of the nearest-neighbor bonds. Eqn.(5) can be represented by a series of summations given by

$$H = \sum_k (a_k^+ \quad b_k^+) \begin{pmatrix} 0 & H_{12}(k) \\ H_{21}(k) & 0 \end{pmatrix} \begin{pmatrix} a_k \\ b_k \end{pmatrix}, \qquad (6)$$

where $H_{12}(k) = -t\left(e^{-ik.e_1} + e^{-ik.e_2} + e^{-ik.e_3}\right) = H_{21}^*(k)$. The dispersion relation with eigenvalues of the Hamiltonian equation satisfies:

$$E(k) = \pm\sqrt{H_{12}(k)H_{12}^*(k)} = \pm t\sqrt{1 + 4\cos\left(\frac{\sqrt{3}a}{2}k_x\right)\cos\left(\frac{3a}{2}k_y\right)4\cos^2\left(\frac{\sqrt{3}a}{2}k_x\right)} \qquad (7)$$

The electron motion of Graphene in the intra-band transition is defined by the Boltzmann equation

$$\frac{\partial f}{\partial t} + \frac{\partial p}{\partial t}.\frac{\partial E}{\partial p}.\frac{\partial f}{\partial E} = \frac{f_0 - f}{\tau} \qquad (8)$$

Where p is momentum of electron and E is the kinetic energy, and τ is the relaxation time. Using the above expression it can be shown that the surface conductivity of Graphene is given by [29]:

$$\sigma^s = \frac{-i}{\omega + i\frac{1}{\tau}} \frac{e^2}{\pi h^2} \int_0^\infty E\left[\frac{\partial f(E)}{\partial E} - \frac{\partial f(-E)}{\partial E}\right] dE + i\left(\omega + i\frac{1}{\tau}\right)\frac{e^2}{\pi h^2}\int_0^\infty E\left[\frac{f(-E)}{(\omega + i/\tau)^2} - \frac{f(E)}{(\omega + i/\tau)^2}\right] - 4(E/\hbar)^2 dE \qquad (9)$$

The in-plane mass permittivity of Graphene is defined as: $\varepsilon_r = 1 + i\sigma^s/(\omega\varepsilon_0 d)$, and σ^s is calculated by the Kubo-formula and can be represented by the surface conductivity. The surface impedance condition of Graphene can be expressed as: $n \times (H_1 - H_2) = \sigma^s E_t$, where H_1 and H_2 are the magnetic fields above and underneath the Graphene sheet, and E_t is the electric field tangential to the Graphene sheet. More details about computational strategies can be found in [29-31].

The production of Graphene required inorganic salts that contain an acetate anion and a metal cation. This polyatomic structure of inorganic salt used here has an ion with a negative charge of one unit and is made up of two carbon atoms which are ionically attached to three hydrogen atoms and two oxygen atoms. The symbol of this polyatomic particle is CH_3COO. Production precursors such as acetic acid are essential to produce nanoscale materials with extremely high purity. The heat conversion method of precursors is employed to produce CuO nanostructures. Heat treatment needs to be performed with due care to preserve the morphological properties of the precursors. Reactions of alkaline compounds such as NaOH with copper salt precursors or copper acetate solution are used to initiate the synthesis process, where Cu ions are reduced to CuO based on this chemical reaction. In the process of making Graphene composites, powder metallurgy is used. In the preparation of composite powders, first the metal powders and Graphene are mixed, then compacted under pressure and heated. Another technique for making Graphene/copper composite powders is by spark plasma sintering (SPS), which is multi-stage and multi-operational process. Evaporation, melting, and sintering are completed within a short time of a few minutes, which involves raising the temperature and pressure. The SPS process concentrates high pulse energy at the point where the grains join is an improvement in sintering over the convective hot press and isostatic hot press processes. In order to obtain copper/ educed Graphene oxide

(Cu/rGO) composite powders, the nanocomposites must be thermally reduced in the H_2 atmosphere and then in SPS to stabilize and consolidate it [21],[32,33]. Fig. 10 illustrate two Graphene production processes.

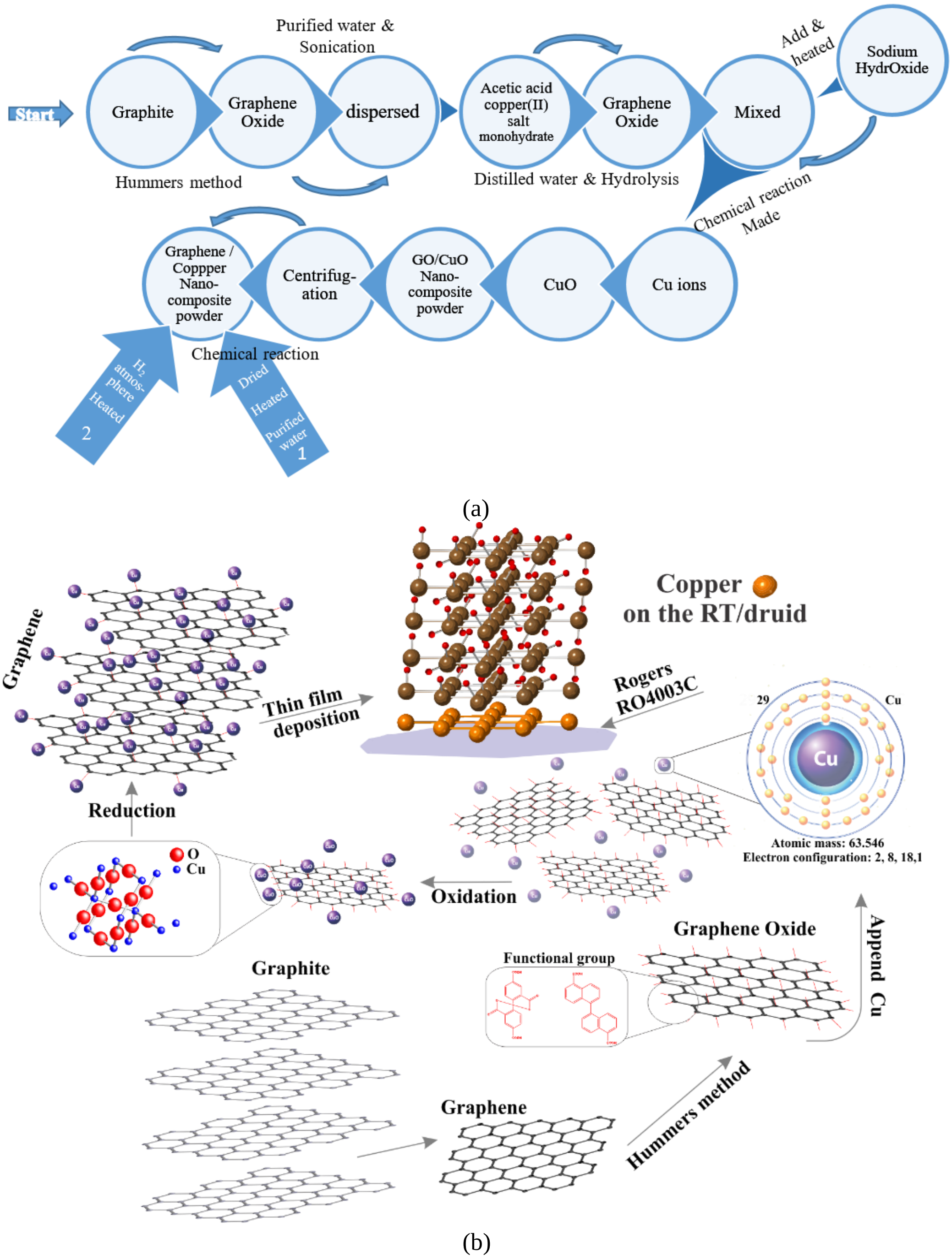

Fig. 10. Schematic of deposition steps, (a) Flowchart of Graphite to Graphene/copper nano composite powder process, and (b) Coating process of Graphene onto Rogers substrate.

Fig. 11 shows the X-ray diffraction (XRD) of the crystalline phase of copper (Cu), Graphene oxide (GO), and copper oxide (CuO) samples. Fig. 12 shows the microstructure of the Graphene without Cu coating and with Cu coating. It can be observed the Graphene oxide sheets are roughly parallel to each other, and the Cu is regularly and uniformly diffused and clung on GO sheets with diameters of a few nanometers.

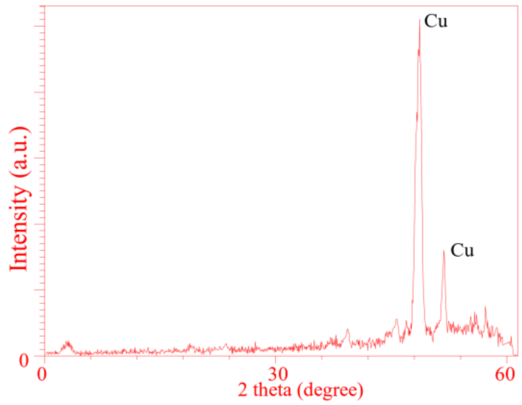

(a)

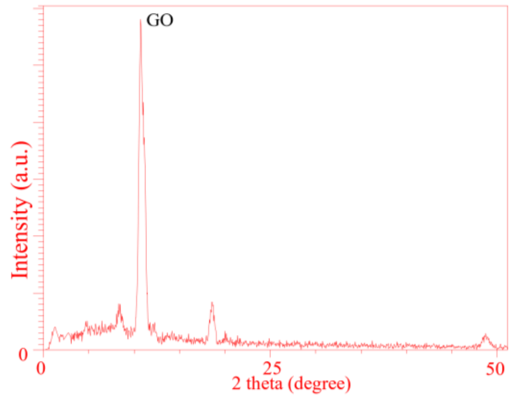

(b)

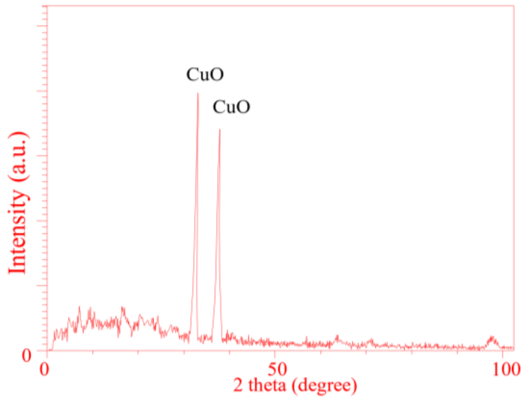

(c)

Fig. 11. X-ray diffraction (XRD) patterns, (a) of the copper, (b) of the Graphene oxide, and (c) of the cupric oxide or copper (II) oxide.

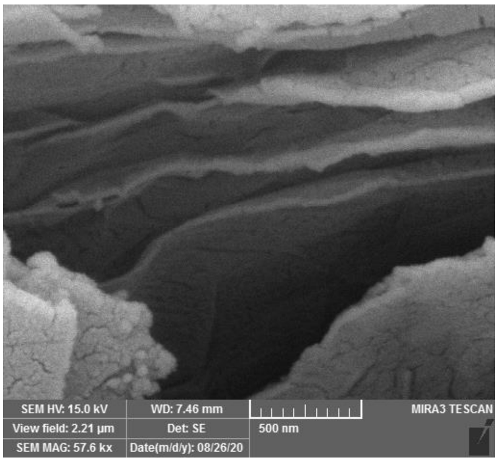

(a)

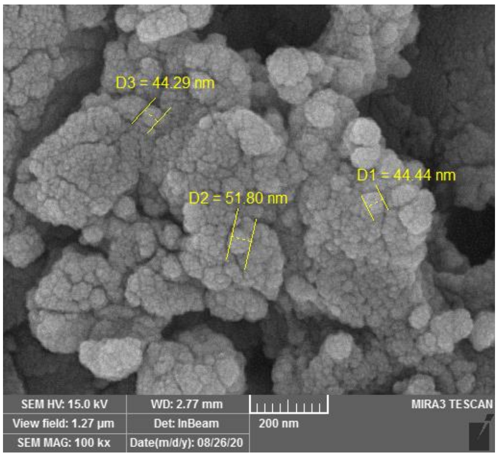

(b)

Fig. 12. Morphology of composite materials, (a) Graphene oxide without Cu coating, and (b) Graphene oxide with Cu coating.

4 Experimental Measurement

The two antenna arrays fabricated are shown in Fig. 13(a) & (b). Ant-1 includes just the CSRR on the HCRS, and Ant-2 includes CSRR and AZIM unit cells on the HCRS. The AZIM consists of a periodic array of open loop meander-lines that are located at the open-end of the tapered slot. Loading of AZIM unit cells onto the CSRR loaded antenna will affect the impedance matching of the antenna. Dimensions and location of the AZIM unit cells on the CSRR was optimized using CST Microwave Studio. The return-loss performance of the arrays was measured using Agilent technologies' E8363C PNA network analyzer, shown in Fig. 13(c). The photograph of the fabricated 1-to-4 Wilkinson power divider (WPD) used in HCRS excitation is shown in Fig. 13(s). Dimensions of the WPD parameters are given in Table 1. The simulated and measured return-loss and antenna gain in the E-plane of Ant-1 and Ant-2 are shown in Fig. 14.

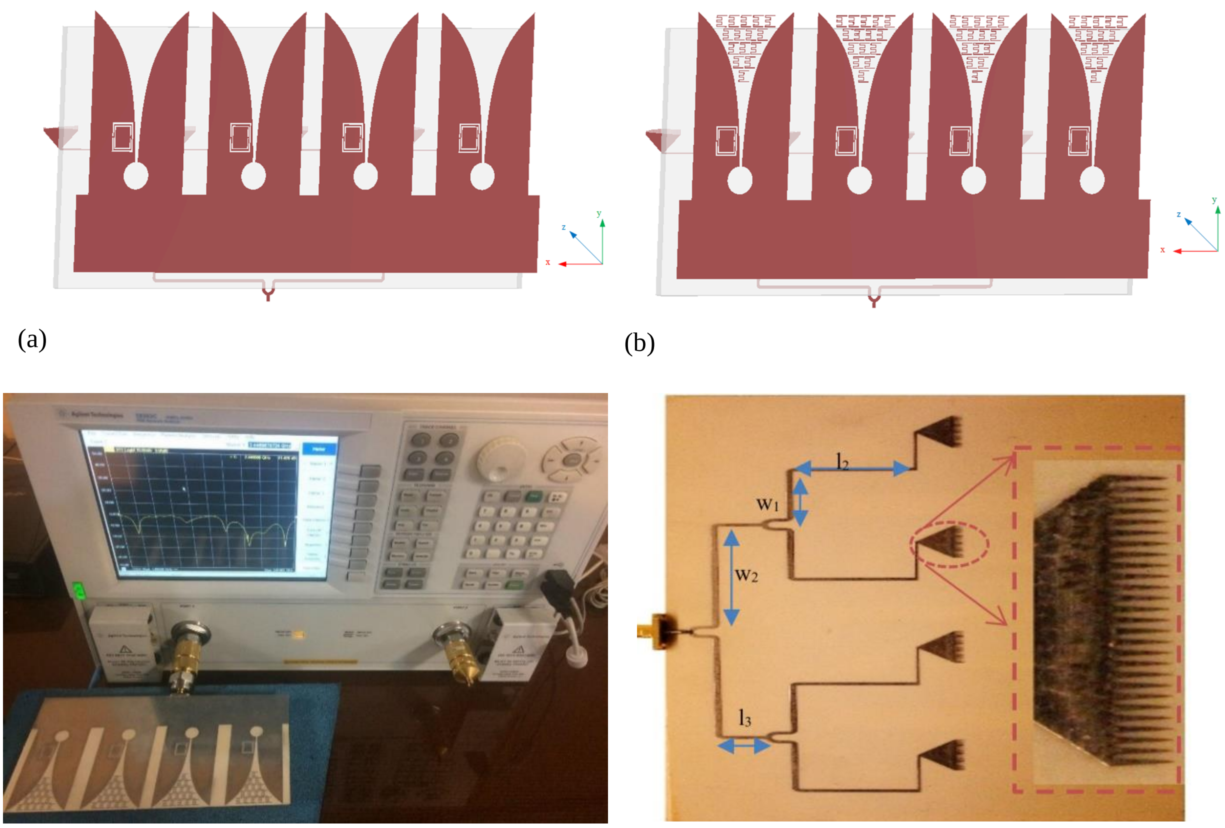

(a) (b) (c) (d)

Fig. 13. CVA designs, (a) Ant-1 with CSRR, (b) Ant-2 with CSRR and AZIM, (c) Measurement setup for Ant-2 with CSRR and AZIM, and (d) Bottom layer of the proposed antenna array with CSRR and AZIM.

Table1: Dimensions of the Wilkinson power divider

Parameter	Value (mm)
w_1	15.63
w_2	20.00
l_1	16.45
l_2	21.95
l_3	7.74

Simulation results show good correlation between Ant-1 and Ant-2. However, the measured results of Ant-2 in Fig. 14(a) show discrepancy with the simulation results, which is attributed to inaccurate Graphene model in EM solver used. The measured results of Ant-2 in Fig. 14(a) shows excellent impedance match (S_{11}<-10 dB) over frequencies 1.15–1.2 GHz, 2.2–2.75 GHz, 2.8–2.95 GHz. There is good correlation in the gain performance of both antennas and the measured results. The peak measured gain is 7.49 dB at 177 degrees and the sidelobes are at least 10 dB below the peak gain. The 3-dB beamwidth of Ant-2 is 32.8 degrees.

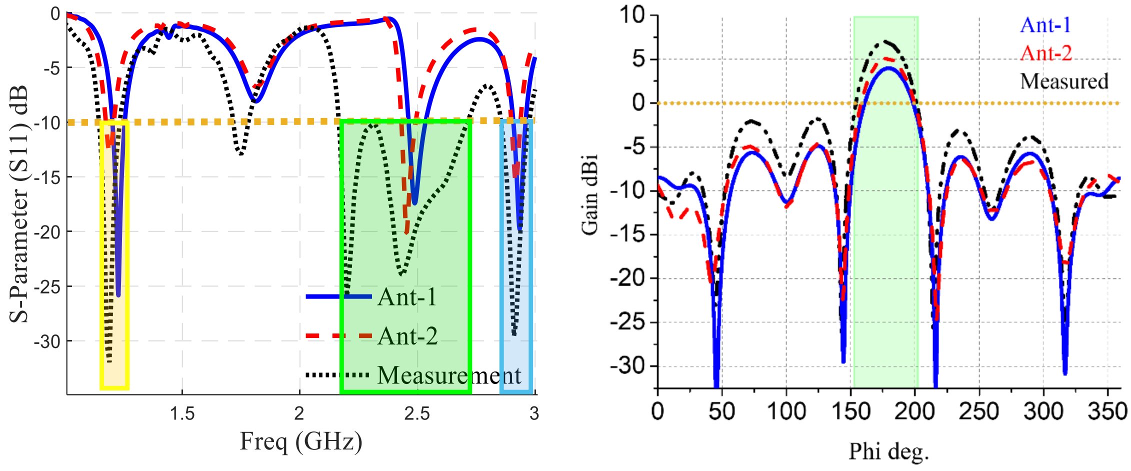

(a) (b)

Fig. 14. Simulated and measured antenna array performance in the E-plane, (a) return-loss of Ant-1 (without AZIM), Ant-2 (with AZIM) and measured response of Ant-2, and (b) Gain pattern of Ant-1 (without AZIM), Ant-2 (with AZIM) and measured response of Ant-2.

The dimensions of CSRR in Ant-2 were modified to resonant at the ISM band of 2.45 GHz. The metallization section of CSRR was coated with a thin-film of Graphene/copper nanoparticles using chemical vapor deposition. This antenna array is referred to as Ant-3. Fig. 15 and 16 show the simulated and measured performance of the Ant-3. Fig. 15 shows the measured return-loss of Ant-3 at 2.45 GHz is better than -40 dB. Fig. 16 shows it has a peak gain of 10 dBi at an angle of 180 degrees, its 3-dB beamwidth is 36 degrees and the sidelobes are at least 15 dB below the peak gain. Gain enhancement of 2.5 dB is observed compared to Ant-2. Fig. 17 shows that Ant-3 radiates unidirectionally over a wide angle (20–150 degrees) in the H-plane. Compared to Ant-2 the sidelobe levels of Ant-3 are noticeably reduced and almost identical radiation pattern is achieved in both E and H-planes. Measurement of the array's radiation pattern was carried out in an anechoic chamber where the ridged horn antenna was used as the reference receiving antenna. Fig. 18 shows the antenna array in the chamber.

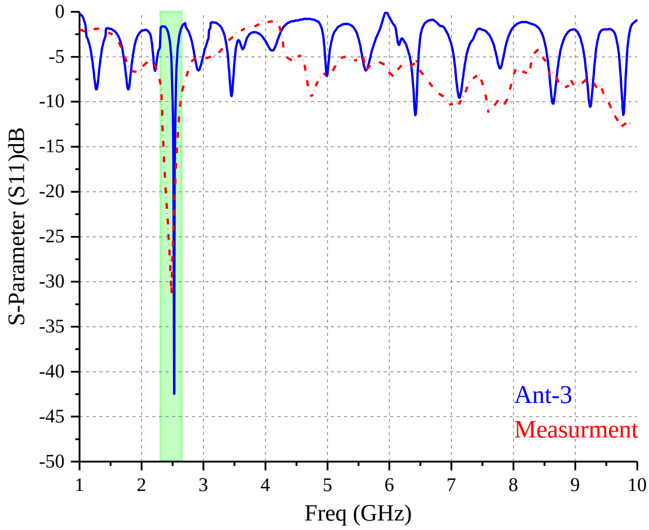

Fig. 15. Simulated and measured return-loss of Ant-3 with Graphene/copper nanoparticle coated CSRR.

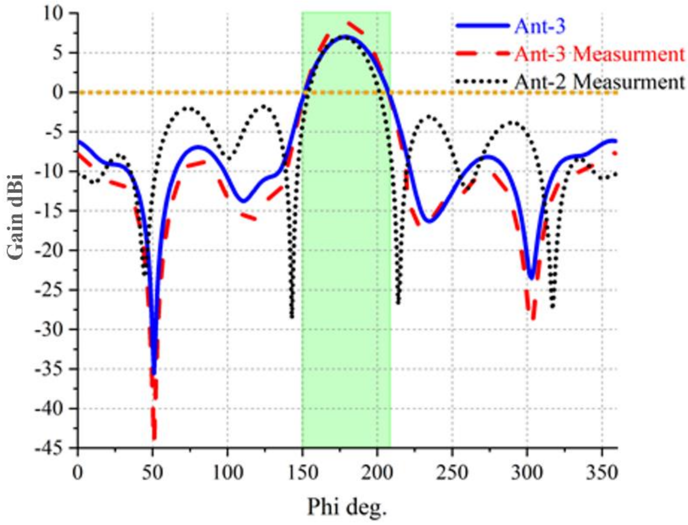

Fig. 16. Simulated and measured gain pattern in the E-plane of Ant-3 with Graphene/copper nanoparticle coated CSRR.

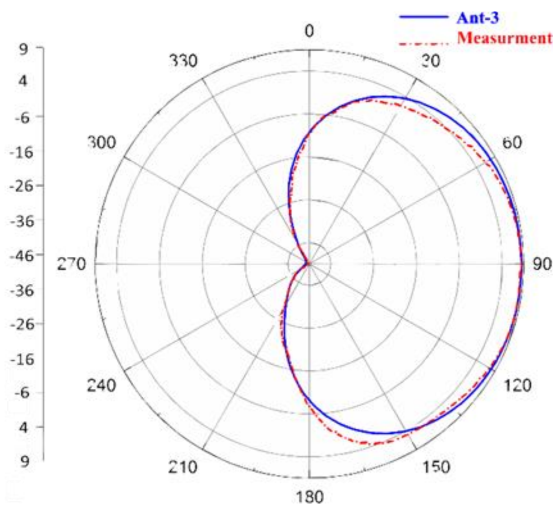

Fig. 17. Radiation pattern of Ant-3 with Graphene/copper nanoparticle coated CSRR in the H-plane.

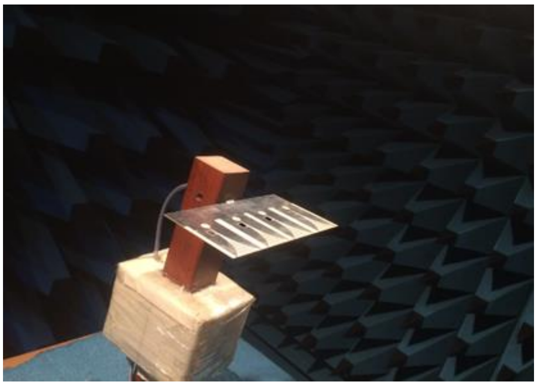

Fig. 18. The proposed antenna under the test in an anechoic chamber.

Conclusions

Experimental results presented here confirm that the gain of a conventional Vivaldi antenna can be increased by loading the antenna with complementary split ring resonators (CSRR) and an array of and open loop meanderline unit cells that are mounted at the open-end of the tapered slot. Furthermore, it is shown that the antenna's performance can be significantly enhanced in terms of gain and radiation characteristics by coating CSRR with a thin film of Graphene/Cu nanoparticles. The proposed technique does not have any impact on the overall dimensions of the antenna. The antenna was excited using a novel feedline with hair-comb radial-stub to ensure optimum coupling. The effectiveness of the proposed technique was verified through simulation and measurement. Vivaldi antennas are used for biomedical imaging applications for detecting malignant tumors due to their highly directional characteristics. The high gain performance of the proposed Vivaldi antenna will result in the use of lower power levels which will therefore reduce the exposure to non-ionization radiation and thus prevent potential tissue damage due to heating effects. The antenna's significantly reduced sidelobes will result in less noise pickup by the imaging system resulting in better resolution of images.

Acknowledgments

The authors would like to thank the Northwest Antenna and Microwave Research Laboratory (NAMRL) at Urmia University for technical support. We would also like to express our gratitude to Dr. Mohsen Karamirad and Dr. Nasrin Mohajeri for fruitful discussions and support of this work.

References

[1] Bin Zhou and Tie Jun Cui, "Directivity enhancement to Vivaldi antennas using compactly anisotropic zero-index metamaterials," *IEEE Antennas Wirel. Propag. Lett.*, vol. 10, pp. 326–329, 2011, doi: 10.1109/lawp.2011.2142170.

[2] M. Bhaskar, E. Johari, Z. Akhter, and M. J. Akhtar, "Gain enhancement of the Vivaldi antenna with band notch characteristics using zero-index metamaterial," *Microw. Opt. Technol. Lett.*, vol. 58, no. 1, pp. 233–238, 2016, doi: 10.1002/mop.29534.

[3] Q.-H. L. Jiangniu Wu, Zhiqin Zhao, "A novel Vivaldi antenna with extended ground plane stubs for ultrawideband applications," *Microw. Opt. Technol. Lett.*, vol. 57, no. 4, pp. 983–987, 2015, doi: 10.1002/mop.28955.

[4] P. J. Gibson, "The Vivaldi aerial," *1979 9th Eur. Microw. Conf.*, doi: 10.1109/EUMA.1979.332681.

[5] P. Piksa, V. Sokol, “Small Vivaldi antenna for UWB,” *Proc. Conf. Radioelektronika*, pp. 490–493, 2005.

[6] E. W. Reid, L. Ortiz-balbuena, A. Ghadiri, and S. Member, “A 324-element Vivaldi antenna array for radio astronomy instrumentation,” *IEEE Trans. Instrum. Meas.*, vol. 61, no. 1, pp. 241–250, 2012.

[7] Thomas J. Ellis and Gabriel M. FLebeii, “MM-Wave tapered slot antennas on micromachined photonic bandgap dielectrics,” *1996 IEEE MTT-S Int. Microw. Symp. Dig.*, 1996.

[8] Y. Wang, G. Wang, and B. Zong, “Directivity Improvement of Vivaldi Antenna Using Double-Slot Structure,” *IEEE Antennas Wirel. Propag. Lett.*, vol. 12, pp. 1380–1383, 2013.

[9] D. M. Elsheakh and E. A. Abdallah, “Compact Shape Of Vivaldi Antenna For Water Detection Using,” *Microw. Opt. Technol. Lett.*, vol. 56, no. 8, pp. 1801–1809, 2014, doi: 10.1002/mop.

[10] D. G. A. Lazaro, R. Villarino, “Design Of Tapered Slot Vivaldi Antenna For Uwb Breast Cancer Detection,” *Microw. Opt. Technol. Lett.*, vol. 53, no. 3, pp. 639–643, 2011, doi: 10.1002/mop.

[11] R. Natarajan, J. V George, M. Kanagasabai, and A. K. Shrivastav, “A compact antipodal Vivaldi antenna for UWB applications,” *IEEE Antennas Wirel. Propag. Lett.*, vol. 14, pp. 1557–1560, 2015, doi: 10.1109/LAWP.2015.2412255.

[12] G. K. Pandey, H. Verma, and M. K. Meshram, “Compact antipodal Vivaldi antenna for UWB applications,” *Electron. Lett.*, vol. 51, no. 4, pp. 308–310, 2015, doi: 10.1049/el.2014.3540.

[13] F. Falcone *et al.*, “Effective negative - epsilon stopband microstrip lines based on complementary split ring resonators,” *IEEE Microw. Wirel. Components Lett.*, vol. 14, no. 6, pp. 280–282, 2004.

[14] S. K. Patel and Y. Kosta, “Triband microstrip–based radiating structure design using split ring resonator andcomplementary split ring resonator,” *Microw. Opt. Technol. Lett.*, vol. 55, no. 9, pp. 2219–2222, 2013, doi: 10.1002/mop.

[15] A. Kabiri, “Artificial magnetic material : limitations, synthesis and possibilities,” A thesis presented to the University of Waterloo 2010.

[16] E. Shamonina, “Basics of single negative and double negative metamaterials.”

[17] M. T. Islam, M. Samsuzzaman, S. Kibria, N. Misran, and M. T. Islam, “Metasurface loaded high gain antenna based microwave imaging using iteratively corrected delay multiply and sum algorithm,” *Sci. Rep.*, vol. 9, no. 17317, 2019, doi: 10.1038/s41598-019-53857-0.

[18] S. K. Tiwari, S. Sahoo, N. Wang, A. Huczko, "Graphene Research and their outputs: status and prospect," *Journal of Science: Advanced Materials and Devices*, vol. 5, issue 1, pp. 10-29, 2020.

[19] X. Yu, H. Cheng, M. Zhang, Y. Zhao, L. Qu, and G. Shi, “Graphene-based smart materials,” *Nat. Rev. Mater.*, vol. 2, pp. 1–14, 2017, doi: 10.1038/natrevmats.2017.46.

[20] S. Bashirvand and A. Montazeri, “New aspects on the metal reinforcement by carbon nanofillers: A molecular dynamics study,” *Mater. Des.*, vol. 91, pp. 306–313, 2016, doi: 10.1016/j.matdes.2015.11.111.

[21] A. M. Lewis, B. Derby, and I. A. Kinloch, “Influence of gas phase equilibria on the chemical vapor deposition of Graphene,” *ACS Nano*, vol. 7, no. 4, pp. 3104–3117, 2013, doi: 10.1021/nn305223y.

[22] P. Hidalgo-Manrique, X. Lei, R. Xu, M. Zhou, I. A. Kinloch, and R. J. Young,

"Copper/Graphene composites: a review," *J. Mater. Sci.*, vol. 54, no. 19, pp. 12236–12289, 2019, doi: 10.1007/s10853-019-03703-5.

[23] R. J. Young, I. A. Kinloch, L. Gong, and K. S. Novoselov, "The mechanics of Graphene nanocomposites: A review," *Compos. Sci. Technol.*, vol. 72, no. 12, pp. 1459–1476, 2012, doi: 10.1016/j.compscitech.2012.05.005.

[24] P. Cataldi, A. Athanassiou, and I. S. Bayer, "Graphene nanoplatelets-based advanced materials and recent progress in sustainable applications," *Appl. Sci.*, vol. 8, no. 9, 2018, doi: 10.3390/app8091438.

[25] P. K. Singh and A. K. Tiwary, "Novel compact dual bandstop filter using radial stub," *Microw. Rev.*, vol. 21, no. 1, pp. 17–22, 2015.

[26] T. Cai, G. M. Wang, X. F. Zhang, Y. W. Wang, B. F. Zong, and H. X. Xu, "Compact microstrip antenna with enhanced bandwidth by loading magneto-electro-dielectric planar waveguided metamaterials," *IEEE Trans. Antennas Propag.*, vol. 63, no. 5, pp. 2306–2311, 2015, doi: 10.1109/TAP.2015.2405081.

[27] S. Zhu, H. Liu, and P. Wen, "A new method for achieving miniaturization and gain enhancement of vivaldi antenna array based on anisotropic metasurface," *IEEE Trans. Antennas Propag.*, vol. 67, no. 3, pp. 1952–1956, 2019, doi: 10.1109/TAP.2019.2891220.

[28] D. Smith, S. Schultz, P. Markoš, and C. Soukoulis, "Determination of negative permittivity and permeability of metamaterials from reflection and transmission coefficients," *Phys. Rev. B*, vol. 65, no. 19, pp. 1–5, 2002.

[29] V. P. Gusynin, S. G. Sharapov, and J. P. Carbotte, "Magneto-optical conductivity in Graphene," *J. Phys. Condens. Matter*, vol. 19, no. 2, 2007, doi: 10.1088/0953-8984/19/2/026222.

[30] M. H. Yu Shao, Jing Jing Yang, "A Review of computational electromagnetic methods for Graphene modeling," *Int. J. Antennas Propag.*, vol. 1, 2016.

[31] R. Wang, X.-G. Ren, Z. Yan, L.-J. Jiang, W. E. I. Sha, and G.-C. Shan, "Frontiers of Physics Graphene based functional devices: A short review," *Front. Phys.*, vol. 14, no. 1, p. 13603, 2019.

[32] N. Djapic and S. Diego, "Method and bend structure for reducing transmission line bend loss," *United States Patent, US6642819B1*.

[33] S. C. Tjong, "Recent progress in the development and properties of novel metal matrix nanocomposites reinforced with carbon nanotubes and Graphene nanosheets," *Mater. Sci. Eng. R Reports*, vol. 74, no. 10, pp. 281–350, 2013, doi: 10.1016/j.mser.2013.08.001.